Journal of the Meteorological Society of Japan

EARLY ONLINE RELEASE

The DOI for this manuscript is
DOI:10.2151/jmsj.2023-018
J-STAGE Advance published date: May 16th, 2023
The final manuscript after publication will replace the preliminary version at the above DOI once it is available.

Comparison of Long-term Total Precipitable Water Products by the Advanced Microwave Scanning Radiometer 2 (AMSR2)

Keiichi Ohara[1], Takuji Kubota[1], Misako Kachi[1],

Japan Aerospace Exploration Agency, Japan

and

Masahiro Kazumori

Japan Meteorological Agency, Japan

November 22, 2022

----

1) Corresponding author: Keiichi Ohara, Earth Observation Research Center, Japan Aerospace Exploration Agency, 2-1-1, Sengen, Tsukuba-shi, Ibaraki 305-8505 JAPAN

Email: ohara.keiichi@jaxa.jp

Tel: +81-50-3362-7730

Fax: +81-29-868-2961

Abstract

This study focused on the total precipitable water (TPW) products of the Advanced Microwave Scanning Radiometer 2 (AMSR2) onboard the Global Change Observation Mission—Water (GCOM-W). The GCOM-W satellite has been flying in the Afternoon Constellation (A-train) orbit to synergize with other A-train satellites, such as Aqua. In this study, we compared two datasets of AMSR2 TPW from July 2012 to December 2020, independently produced by the Japan Aerospace Exploration Agency (JAXA) and Remote Sensing Systems (RSS). There were no significant differences in TPW anomaly trends between them. However, significant differences in the absolute values of TPW were found in the northwest Pacific and northwest Atlantic Oceans during the boreal summer season. We investigated the meteorological conditions that caused these differences using reanalysis, in-situ observation data, and visible and infrared data from the MODerate resolution Imaging Spectroradiometer (MODIS) on the Aqua. The results showed that the lower atmosphere had an inversion layer with relative humidity close to 100%, and very low altitude clouds (i.e., fog) were often distributed in the areas where the TPW differences between JAXA and RSS are large. The temperature profiles represented in the JAXA and RSS algorithms were approximated by a simple model. The influence of the inversion layer and fog on the JAXA and RSS TPW algorithms was also investigated using a radiative transfer model. Sensitivity experiments suggested that the inversion layer was associated with the underestimated TPW for the JAXA algorithm, while it was associated with the overestimated TPW for the RSS algorithm.

Keywords GCOM-W/AMSR2, Water vapor content, Comparison and validation, Long-term analysis, Inversion layer, Sea fog

1. Introduction

Water vapor is the most important greenhouse gas and causes significant positive feedback to global warming (Held and Soden 2000; Zhai and Eskridge 1997; Wagner et al. 2006). The Intergovernmental Panel on Climate Change (IPCC) Working Group I (WG I) Sixth Assessment Report (AR6), released in August 2021, concluded from observations, reanalysis, and models that total precipitable water vapor (TPW) has *very likely* increased since 1979 and that the combined water vapor and lapse rate feedback makes the single largest contribution to global warming (IPCC 2021). Variations in water vapor content also significantly impact the global energy balance and other climate systems, such as clouds and precipitation, through absorption and release of latent heat (Trenberth et al. 2003, 2009). Thus, water vapor is key to understanding the mechanisms of global climate and water cycle changes. Observing and analyzing water vapor continuously and homogeneously is essential on a global scale over an extended period.

There are three principal methods for determining water vapor content: in-situ observation using radiosondes (Dai et al. 2011; Zhai and Eskridge 1997), estimation from zenith path delay (ZPD) of Global Positioning System (GPS) observations (Wang et al. 2007; Nilsson and Elgered 2008), and remote sensing using satellites (Wentz and Schabel 2000; Wagner et al. 2006). Water vapor observations by radiosonde and ground-based GPS are highly accurate, and many studies of water vapor trends have been conducted using these methods. In particular, radiosonde observation data have been accumulated over a long time, and the IPCC Third Assessment Report listed water vapor trends at radiosonde stations in the northern hemisphere (Ross and Elliott 2001). However, radiosonde and ground-based GPS observation data are limited to land, small isolated islands, and ships, so the spatiotemporal inhomogeneity of the data has been noted as a disadvantage (Dai et al. 2011). Satellite-based remote sensing is suitable for global climate studies because it provides data that are more spatiotemporally homogeneous than radiosonde or GPS-based observations. Observations by passive microwave radiometers are less affected by clouds, unlike those by visible and infrared sensors (Wagner et al. 2006), even though they are made chiefly over oceans. In addition, multiple satellites have made microwave observations continuously since 1979 (Mears et al. 2018; Kidd et al. 2021). Thus, data from spaceborne passive microwave radiometers are important for monitoring long-term global water vapor. Indeed, the IPCC Fourth, Fifth, and Sixth Assessment Reports provide TPW trends over the ocean using microwave satellite data (IPCC 2007, 2013, 2021).

Previous studies reported estimates of global water vapor trends: 0.436 ± 0.10 kg m^{-2} decade^{-1} for 1988–2011 (microwave satellites; Mears et al. 2018); 0.34 ± 0.10 (microwave satellites), 0.22 ± 0.28 (radiosonde), 0.34 ± 0.26 (GPS), 0.34 ± 0.14 (reanalysis data from the European Centre for Medium-Range Weather Forecasts), and 0.27 ± 0.18 kg m^{-2} decade^{-1} (reanalysis data from National Centers for Environmental Prediction) for 2000–2014 (Chen and Liu 2016); and 0.50 (ultraviolet and visible satellites), 0.24 kg m^{-2} decade^{-1} (reanalysis data from Hamburg Ocean Atmosphere Parameters and Fluxes from satellite data) for 1996–2005 (Mieruch et al. 2014). IPCC AR6 WG1 reported that the global TPW trend is *very likely* to be positive (since 1979) because various satellites have enabled a quasi-global assessment of total column water vapor. On the other hand, it is noted that the estimation of the magnitude of the TPW trend requires *medium confidence* due to the uncertainties associated with changes in observation systems. The uncertainty caused by changes in observation systems is also examined in the Global Energy and Water Cycle Exchanges project (GEWEX) water vapor assessment (G-VAP) (Schröder et al. 2016, 2018, 2019). G-VAP is a framework for comprehensively comparing water vapor datasets, including satellite and reanalysis data. It was reported that the differences in water vapor trends among datasets are caused primarily by different breakpoints in the data, which often coincide with changes in the observation systems or the data used for assimilation (Schröder et al. 2016, 2019). Therefore, more accurate and consistent long-term datasets from single or series satellites are needed for more accurate estimates of water vapor trend values.

The Advanced Microwave Scanning Radiometer 2 (AMSR2) is a Japanese conical scanning passive microwave radiometer on board the Global Change Observation Mission—Water (GCOM-W) satellite, or SHIZUKU. GCOM-W was launched from the Tanegashima Space Center on May 18, 2012 (Imaoka et al. 2010). The GCOM-W satellite moved into the orbit on June 29, 2012 as one of the A-train satellites for synergistic observations around 1:30 PM local solar time by multiple Earth observation satellites, such as Aqua. GCOM-W/AMSR2 has been making observations for more than 10 years, since June 2012, as the successor to Aqua/AMSR-E (2002–2011) (Kawanishi et al. 2003). In addition, GCOM-W/AMSR2 is almost independent of weather conditions and has a wide observation swath of 1450 km, making it possible to observe more than 99% of the Earth every two days. The TPW over the ocean can be retrieved from AMSR2 observation data (Kazumori et al. 2012; Wentz 2000). Therefore, the global and long-term observations of GCOM-W/AMSR2 are important for studying the water vapor trend.

This study aims to compare and validate the AMSR2 TPW product of the Japan Aerospace Exploration Agency (JAXA) and the Remote Sensing Systems (RSS) with each other. The TPW products by the RSS were also used in the IPCC report to evaluate reanalysis data and models (Wentz et al. 2007). We investigated the TPW differences between JAXA and RSS for time series, location, and seasonal dependence. The study also investigated meteorological conditions that could cause these TPW differences using data from radiosondes, objective analysis, and observations of visible and infrared imagers onboard the A-train satellite. Section 2 describes the data used in this study and the matching process with radiosonde observations. Section 3 describes the seasonal and regional dependence of TPW differences between RSS and JAXA. Section 3 also describes the TPW anomaly trend from JAXA and RSS products. Section 4 describes the causes of the principal TPW differences. Section 5 summarizes this paper and describes the direction for our planned research.

2. Data

2.1 JAXA AMSR2 product

The AMSR2 is carried by the GCOM-W satellite (Imaoka et al. 2010). The diameter of the main reflector of AMSR2 is 2 m, the largest of all conical scanning microwave radiometers currently on board satellites. This large reflector allows AMSR2 to make high-resolution observations (the footprint is 7×12 km at 36.5 GHz). In addition, AMSR2 covers a wide range of frequencies (6,925, 7.3, 10.65, 18.7, 23.8, 36.5, and 89.0 GHz) and V/H polarization (14 channels). Thus, AMSR2 can estimate various geophysical parameters such as water vapor, cloud liquid water, precipitation, sea surface temperature, surface wind speed, sea ice concentration, snow depth, and soil moisture (see Descriptions of GCOM-W1 AMSR2 Level 1R and Level 2 Algorithms, https://suzaku.eorc.jaxa.jp/GCOM_W/data/doc/NDX-120015A.pdf.).

This study used JAXA's daily product (AMSR2 Standard Product Level 3 ver. 2, 0.25° grid) for data between July 2012 and December 2020 in the long-term analysis and comparison of TPW products. The daily product contains daily averaged data for the ascending orbit observed at 13:30 local time and the descending orbit observed at 1:30 local time; both data were used in this study. As described below, JAXA AMSR2 Standard Product Level 2 ver. 2 was used in the matchup process with the radiosonde data. The Level 2 data is swath data that is not gridded and has location information associated with each observation point.

The JAXA AMSR2 TPW algorithm is outlined as follows. The JAXA algorithm estimates the TPW by an iterative process (Kazumori et al. 2012), using the MGDSST (see Section 2.5), sea surface wind speed (SSW), and 850 hPa air temperature of GANAL (see Section 2.4) interpolated to the same location and time as the AMSR2 observations. The sea surface emissivity is estimated with the first Look Up Table (LUT) using GANAL SSW and MGDSST as ancillary data for each observation frequency. The atmospheric transmittance is estimated with the second LUT using the 850 hPa air temperature and brightness temperatures of 18.7, 23.8, and 36.5 GHz. The TPW and cloud liquid water (CLW) can be estimated from the atmospheric transmittance in the third LUT. The above LUTs are created by a dataset of the radiosonde observations, MGDSST, and GANAL SSW in advance.

2.2 RSS AMSR2 product

RSS's AMSR2 TPW products were compared to JAXA's AMSR2 TPW products. The RSS TPW was estimated using an algorithm developed independently by RSS (Wentz 2000, 2007). RSS is a private U.S. company that collects, processes, and analyzes data from spaceborne microwave radiometers. The RSS products used in this study were the Level 3 ver. 8.2 (0.25º grid) Daily Products from July 2012 to December 2020. The RSS Daily Products also contain daily averaged data for ascending and descending orbits, respectively.

The RSS AMSR2 TPW algorithm, the Ocean algorithm, uses regression equations for retrieval and can estimate SST, SSW, and CLW simultaneously (Wentz 2000, 2007). The regression coefficients that connect the geophysical parameters and brightness temperatures were derived from the brightness temperature dataset calculated in advance. This dataset is calculated from the radiosonde atmospheric profiles, assumed sea surface parameters, and cloud layers by the radiative transfer model. SSW, CLW, and cloud altitude are randomly varied within realistic value ranges, and SST is randomly varied based on Reynolds SST around island site of radiosonde.

2.3 Radiosonde observations

Radiosonde observations are a meteorological observation network that is routinely conducted by meteorological agencies around the world. Radiosonde observation networks are used internationally by the Global Telecommunication System (GTS). Radiosondes can directly measure meteorological parameters such as atmospheric pressure, air temperature, and relative humidity at various altitudes using balloons. Since TPW is vertically integrated water vapor, it can be calculated from the integrated observation data at each altitude. In this study, radiosonde data for 2013−2020 were used for validation.

Radiosonde and AMSR2 data used for verification were selected based on observation time, the distance between observation points, quality, and uniformity. The selection method is as follows. First, AMSR2 Level 2 TPW data with observation time differences of less than 1 h and distance of less than 30 km from radiosonde observations were collocated. Next, the radiosonde and AMSR2 data were left as candidates for matching up data only when the AMSR2 Level 2 TPW data collocated around radiosonde data contain at least five good-quality data samples (Quality Control is 0), and the maximum difference of AMSR2 data was less than 5 kg m^{-2}. This is the same validation method routinely employed by JAXA (see the JAXA homepage: https://suzaku.eorc.jaxa.jp/cgi-bin/gcomw/validation/gcomw_validation_tpwi2.cgi). We used the JAXA Level 2 data in the above process because JAXA Level 2 TPW products are available, but RSS are not. Last, the nearest JAXA and RSS Level 3 TPW data from the radiosonde observations selected in the above procedure were searched within 60 km. Because observation paths cross during the day, especially at high latitudes, the data observed at different times were averaged on the same grid when generating the L3 daily product from the L2 data. Here, we excluded the grid where different time observations were averaged.

2.4 GANAL

Global ANALysis data (GANAL) is the global objective analysis data of the Japan Meteorological Agency (JMA). GANAL data are produced every 6 hours on a 0.5° equirectangular grid (see Outline of the Operational Numerical Weather Prediction at the Japan Meteorological Agency: https://www.jma.go.jp/jma/jma-eng/jma-center/nwp/outline2023-nwp/index.htm). In this study, we used daily mean SSW data (averaged 00, 06, 12, and 18 UTC data), relative humidity at various altitudes, and temperature at various altitudes from GANAL for 2018.

2.5 MGDSST

Merged satellite and in-situ data Global Daily Sea Surface Temperature (MGDSST) (Sakurai et al. 2005) is a global daily SST product of JMA. MGDSST is a global 0.25° equirectangular grid of SST estimated from multiple satellite data, such as infrared sensors and microwave radiometers, and in-situ observations by buoys and ships. In this study, we used data for 2018.

2.6 NASA MODIS product

The Aqua MODerate resolution Imaging Spectroradiometer (MODIS) is a visible and infrared imaging radiometer on board the Aqua satellite in A-train orbit. The A-Train satellites, including GCOM-W and Aqua satellites, provide almost simultaneous observations of the same location, facilitating studies using multiple sensors. This study used Surface Reflectance and Cloud Properties products from Daily Level-3 products for July and August 2018. The resolution is a 0.05º grid for Surface Reflectance and a 1º grid for Cloud Properties.

3. Comparison of JAXA and RSS TPW products

3.1 Differences in temporal and horizontal distributions of TPW

This section compares temporal and horizontal distributions of JAXA and RSS AMSR2 TPW products. Figure 1 shows the time series of the global monthly mean of AMSR2 TPW for JAXA (red) and RSS (blue) over the ocean from July 2012 to December 2020. The global monthly mean of JAXA TPW is smaller than that of RSS over the entire period.

We analyzed the latitudinal zonal mean differences to investigate the differences between JAXA and RSS products found in Fig. 1. Figure 2 shows the time series of TPW product differences between RSS and JAXA, classified by the Northern Hemisphere (NH) mid-latitudes, the low latitudes, and the Southern Hemisphere (SH) mid-latitudes. It can be found that the latitudinal zonal mean of the TPW differences (RSS - JAXA) for the NH mid-latitudes (red) have large value of over 2 kg m^{-2} every boreal summer. That of the low latitudes and the SH mid-latitudes (green and blue) show smaller seasonal variations than NH mid-latitudes (red). In these regions (green and blue), the magnitude of the mean of TPW differences is about 1 kg m^{-2}.

To further examine the seasonal and regional dependences of the TPW differences, we investigated the seasonal variation of the horizontal distribution of the TPW differences. Figure 3 shows the regional dependences of TPW differences averaged over January, April, July, and October for 2013–2020. We used only the grid points estimated by both the JAXA and RSS Daily products in averaging. It can be found that only the data in July have large TPW differences of nearly 5 kg m^{-2} in the northwest Pacific and northwest Atlantic at 30º–60°N. A similar tendency was observed for the TPW differences in other boreal summer months, such as June and August (not shown). In other regions and seasons, the seasonal variation of the horizontal distribution of the TPW differences is relatively small, and the magnitude of TPW differences is about 1 kg m^{-2}. Therefore, we separately discuss the large TPW differences seen in boreal summer in the NH mid-latitudes and the small TPW difference, which is season- and location-independent.

3.2 Validation with radiosonde observations

We compared and verified the accuracy of the JAXA and RSS TPW products using radiosonde observations. The comparisons were performed in the following two cases of seasons and regions. The first is a global comparison during all seasons of 2012–2020 (case A), and the second is a comparison of the NH mid-latitudes (30º–60º N, 120º E–30º W) during the boreal summer (July and August) of 2012–2020 (case B). The season and region of case B are those for which large TPW differences are seen in Fig. 3. Figure 4 shows the distribution of the matched data collocated using the method of Section 2.3. For case A, there are 390 matched radiosonde sites and 4430 matched radiosonde observations. However, for case B, the number of matched radiosonde sites and the number of matched radiosonde observations are 23 and 252, respectively. The size of the plotted points in Fig. 4 indicates the number of observations at the same site.

Figure 5 compares radiosonde and AMSR2 L3 TPW products of JAXA and RSS for case A. The value of the color bar indicates the number of matchup data that fall into the same bin. The mean bias and RMSE against the radiosonde TPW observation values are shown in Table 1. Bias=-0.369, RMSE=2.907 kg m^{-2} for the JAXA TPW product and bias=0.448, RMSE=2.770 kg m^{-2} for the RSS TPW product were obtained. The absolute values of mean bias and RMSE for the JAXA and RSS products are almost equal (almost the same accuracy), but the signs of the mean bias are opposite. The TPW difference is 0.448-(-0.369)=0.817, taking the difference in mean bias from the radiosonde. This value is consistent with the season- and location-independent difference of about 1 kg m^{-2} between RSS and JAXA TPW products, as shown in Figs. 2 and 3. Therefore, this season- and location-independent TPW difference of about 1 kg m^{-2} is likely due to a combination of small systematic errors of less than 0.5 kg m^{-2} in both JAXA and RSS products. As shown in Section 2, the JAXA algorithm estimates the TPW based on LUTs, which are created from the radiosonde observations, MGDSST and GANAL SSW. The RSS algorithm estimates the TPW based on regression equations created from the radiosonde atmospheric profiles, randomly assumed sea surface parameters and cloud layers. The causes of the systematic errors may be due to the differences in the methods (LUTs or regression) used in the two algorithms and the difference in the location and period of the in-situ observation data used to develop the TPW algorithm.

The result of comparing radiosonde and AMSR2 L3 TPW products for case B is shown in Fig. 6. The mean bias and RMSE against radiosonde TPW observations are bias=-0.605, RMSE=2.312 kg m^{-2} for the JAXA TPW products and bias=1.498, RMSE=2.678 kg m^{-2} for the RSS TPW products. For both JAXA and RSS TPW products, the absolute value of mean bias is larger than the result for case A shown in Fig. 5. The mean bias of the JAXA TPW product is slightly smaller than that of the RSS TPW product. However, it should be noted that the number of matched data in the boreal summer of the NH mid-latitudes is much smaller than in global and all seasons, and the number of matched radiosonde sites is limited (shown in Fig. 4). The difference in mean bias between RSS and JAXA is 1.498-(-0.605)=2.103, corresponding to the large TPW differences of over 2 kg m^{-2} found in Figs. 2 and 3. We discuss a probable reason for this large TPW difference in Section 4.

3.3 Long-term trends of TPW anomalies for JAXA and RSS products

In the previous subsection, we discussed the differences in absolute values of JAXA and RSS TPW products that change within a year. In this subsection, we investigate whether there are differences in the long-term trends of water vapor anomalies. The results from the investigation are important for climate studies using JAXA or RSS TPW products.

Figure 7 shows the time series of the anomalies of the TPW global mean for JAXA and RSS products. To exclude seasonal variations of TPW, the anomalies were calculated by subtracting the monthly climate value from the monthly mean value for each product (JAXA and RSS). JAXA and RSS TPW products showed little difference in long-term anomaly trends, although the absolute values of TPW were different (shown in Fig. 1). The linear regression lines and their slopes (kg m^{-2} $decade^{-1}$) are shown for each time series observation in Fig. 7. The values of the water vapor trend for JAXA and RSS products are JAXA ascending, 0.38 ± 0.14 kg m^{-2} $decade^{-1}$; RSS ascending, 0.44 ± 0.13 kg m^{-2} $decade^{-1}$; JAXA descending, 0.41 ± 0.14 kg m^{-2} $decade^{-1}$; and RSS descending, 0.43 ± 0.13 kg m^{-2} $decade^{-1}$. The method for calculating slope and error values was based on Chen and Liu (2016). TPW trend values for microwave satellites in previous studies analyzed over a period that partially overlapped the AMSR2 observation period were reported to be 0.436 kg m^{-2} $decade^{-1}$ (Mears et al. 2018) and 0.34 ± 0.10 kg m^{-2} $decade^{-1}$ (Chen and Liu 2016). These are close to or within the error range of the value obtained by this study. In addition, the large anomaly values seen during 2015 and 2016 are likely due to the El Niño that occurred from the boreal summer of 2014 to the spring of 2016 (see JMA homepage: https://www.data.jma.go.jp/gmd/cpd/data/elnino/learning/faq/elnino_table.html). Positive water vapor anomalies corresponding to El Niño have been reported in other periods (Mieruch et al. 2008).

Figure 8 shows the horizontal distribution of water vapor trends of JAXA and RSS TPW products calculated for each 1° grid to examine the regional dependence of the water vapor trend. The dotted regions indicate significant trends at the 95% confidence level calculated by the t-test (Chen and Liu 2016). Although only the ascending data is shown in the figure, the descending data indicate almost the same results (not shown). The regional dependences of the long-term anomaly trends for JAXA and RSS TPW products also show negligible differences. Compared to previous studies, the patterns of water vapor trends are not perfectly consistent because of the different analysis periods. However, trends such as alternating positive and negative zonal patterns symmetric to the equator are common (Wang et al. 2016; Mears et al. 2018; IPCC 2013).

4. Discussion

This section discusses the possible reasons for the large TPW differences (RSS - JAXA) observed in the northwest Pacific and northwest Atlantic Oceans during the boreal summer. Based on the principle of microwave radiative transfer, the primary error factors in TPW retrieval by passive microwave radiometers are sea surface physical quantities (sea surface temperature and sea surface wind speed), atmospheric physical quantities (cloud water, air temperature, and humidity), or a combination of these quantities. The sea surface quantities serve as background radiation, and the atmospheric quantities affect microwave radiation transmission. In previous research, significant warm air advection was known as the characteristic meteorological field in the northwest Pacific and northwest Atlantic Oceans during the boreal summer (Kubar et al. 2012). In the northwest Pacific, during the boreal summer, the southwest winds are dominated by the Pacific High, resulting in warm and moist air being transported to a much colder sea surface across the SST front near the Kuroshio Current (Norris and Leovy 1994; Kubar et al. 2012). This warm air advection is known to cause fog which frequently occurs at north of the SST front (Klein and Hartmann 1993; Norris and Iacobellis 2005). These warm air advection and fog make it possible to affect microwave observations and TPW retrievals.

With this background in mind, we investigated the relationship between the TPW difference and the atmospheric and oceanic physical parameters, including the physical quantities related to atmospheric stability above the sea surface. In this study, we used MGDSST, GANAL SSW (2 m above the sea surface), and JAXA's CLW products, which are used as input or output data in the JAXA TPW algorithm (Kazumori et al. 2012). The RSS AMSR2 SST, SSW, and CLW products, which are retrieved together with TPW by RSS Ocean Algorithms (Wentz 2000), were also used. The atmospheric profile data (temperature and humidity) were obtained from GANAL. We also focused on the difference between sea surface temperature (MGDSST) and GANAL air temperature at 1000 hPa (T_{1000}) as an indicator of atmospheric stability. Relative humidity at 1000 hPa (RH_{1000}) was used as an indicator of the near-surface moistening.

4.1 Correlation analysis

Spatial correlations between TPW differences and other physical quantities related to microwave radiation were investigated. Table 2 shows the pattern correlation coefficients between TPW differences and the other physical quantities for the global and 30º–60° N ranges, respectively. The pattern correlation coefficients were calculated by comparing the two-month average horizontal distributions of each geophysical quantity for July and August 2018. The values in Table 2 show that the differences between GANAL T_{1000} and MGDSST (T_{1000}-SST) and GANAL RH_{1000} correlate strongly with the TPW differences; the absolute value of the pattern correlation coefficient is above 0.5 for the global and about 0.7 for the 30°−60°N ranges. The horizontal distributions of TPW difference (a), T_{1000}-SST (b), and RH_{1000} (c) are shown in Fig. 9. The horizontal distributions of T_{1000}-SST and RH_{1000} show a characteristic pattern in NH mid-latitudes. This pattern is similar to TPW differences in Fig. 9a. The spatial distributions of other physical quantities in Table 2 are not shown in Fig. 9. These have a characteristic pattern not only for the NH mid-latitudes but also for tropics and SH. Therefore, in Table 2, CLW, MGDSST, and SSW differences also have high correlation coefficients at 30º-60°N (above 0.5) but low correlation coefficients at the global level (below 0.5). Here we focus on T_{1000}-SST and RH_{1000}, which have high correlation coefficients (above 0.5) for both globally and at 30º-60°N. Focusing on these regions with large TPW differences, Fig. 10 shows scatter plots of the relationship (a) between TPW difference and T_{1000}-SST and (b) between TPW difference and RH_{1000}, respectively, using only the 30º–60°N region data for July and August 2018. Figures 9b and 10a show that the TPW difference tends to be large in the T_{1000}-SST > 0 region. Figures 9c and 10b show that the TPW differences tend to increase as RH_{1000} increases. These meteorological conditions, where T_{1000} is warmer than SST and RH_{1000} is very high, are consistent with the characteristic warm air advection and sea fog in the northwest Pacific in boreal summer shown by previous studies (Norris and Leovy 1994; Kubar et al. 2012).

The seasonal and regional dependences of the frequency of the above characteristic cases (T_{1000}>SST and RH_{1000}~100%) were investigated. For the detail, the number of occurrences that satisfy T_{1000}-SST > 2°C and RH_{1000}>95% was counted for each grid point in January, April, July, and October of 2018. The results for each month are shown in Fig. 11. The frequency of the cases that satisfy T_{1000} -SST>2°C and RH_{1000}>95% occur most frequently in July in the northwest Pacific and northwest Atlantic. It is also found that the regional and seasonal dependences of the frequency in Fig. 11 are similar to those of the TPW differences in Fig. 3.

4.2 Investigation of atmospheric vertical profile

Previous studies have reported that when subtropical warm moist air is advected to the cold sea on the polar side, the lower atmosphere becomes more stable, which suppresses cumulus development and allows fog and lower-level clouds to form and persist at lower altitudes (Norris and Iacobellis 2005; Klein and Hartmann 1993). The averages of the atmospheric vertical profiles were calculated to investigate the atmospheric stability in regions with large TPW differences. Figure 12 shows the averages of the atmospheric vertical profiles in the 30º−60° N region for July and August 2018, classified by TPW difference values. Here, the daily mean atmospheric profiles of GANAL are averaged over two months of data. The TPW difference ΔV kg m^{-2} is divided into ΔV>5 (red),

$4<\Delta V<5$ (yellow), $3<\Delta V<4$ (green), $2<\Delta V<3$ (light blue), $1<\Delta V<2$ (blue) and $\Delta V<1$ (black). From Fig. 12a, the humidity profile for a larger TPW difference has the greater relative humidity in the lower atmosphere, which is close to 100%, indicating meteorological conditions suitable for fog formation. Focusing on the air temperature profile (Fig. 12b), the temperature lapse rate in the lower atmosphere becomes smaller as the TPW difference increases. In particular, the temperature lapse rate between 925 and 1000 hPa is negative for $\Delta V>5$. To discuss the atmospheric stability, the equivalent potential temperature profile was also calculated from the relative humidity and temperature profiles (Fig. 12c). The equivalent potential temperature profile indicates that the more stable inversion layer is formed in the lower atmosphere at the large TPW difference region. When fog is present over the ocean, this inversion layer helps to maintain fog in the lower atmosphere. To clear up the dependence of the atmospheric profiles on the TPW difference, this analysis was limited to the range of typical TPW values (30–50 kg m^{-2}) in the mid-latitude range. The results for all TPW values are not shown, but the tendencies described above remain the same. Whether fog occurs over the ocean is discussed in Section 4.3.

The same analysis as above was performed using matched radiosonde atmospheric profile data. The matching details are given in Sections 2.3 and 3.2. Although the number of comparison data of radiosonde is less than that of GANAL data, radiosonde data have advantages that they are actual observations and have higher vertical resolution than GANAL. Four examples of atmospheric profiles observed by radiosonde on different days in July and August at Shemya Island, located at 52.72° N and 174.10° E, are shown in Fig. 13(a). In the examples shown in blue and green solid lines, the radiosonde-matched AMSR2 TPW difference (RSS- JAXA) is small (ΔV = 1.16 and 1.45 kg m^{-2}, respectively), while in the examples shown in yellow and red solid lines, the TPW difference is large (ΔV = 4.73 and 6.30 kg m^{-2}). In the cases with larger TPW differences (yellow and red), there is a temperature inversion layer in the lower atmosphere, and the lower atmosphere has 100% relative humidity. In comparison, there is no such trend for smaller TPW differences (blue and green) cases. Figure 13(b) shows the average radiosonde atmospheric profiles classified by the TPW difference. Here, the data were averaged and plotted every 20 hPa. As in Section 3.2, the period of data is the boreal summer (July and August) of 2012–2020 for the NH mid-latitudes (30º–60 º N, 120 º E–30 º W). Although some of the data have a large noise, the atmospheric profiles of radiosondes show that the relative humidity is very high in the lower atmosphere and that an inversion layer is formed in the large TPW difference cases. These results for radiosonde have the same tendency as the results for GANAL (shown in Fig. 12).

4.3 Evidence of fog occurrence

The analyses in the previous sections have shown that the meteorological conditions are favorable for the development and maintenance of fog in the region where the TPW differences are large. In this subsection, we use MODIS data to examine the relationship between cloud characteristics and TPW differences. The local time of observation of MODIS is almost the same as that of AMSR2 because both are in A-train orbit. Figure 14 shows the AMSR2 TPW difference (a) and MODIS visible

(b) and infrared (c) images (merged daily) on August 2, 2018. In general, fog and lower clouds are optically thicker in the visible region and, therefore, brighter (whiter) in the visible image. On the other hand, fog and lower clouds have higher cloud-top temperatures due to their lower cloud tops and thus appear warmer (blacker) in the infrared image. In the region where the TPW differences are large (Fig. 14a), some convective cloud areas are bright in both visible and infrared images (Figs. 14 b and c), but the fog and lower cloud areas that are bright in the visible image and dark in the infrared image also widely spread.

Statistical analyses were performed using MODIS cloud products to clarify the relationship. Figure 15 shows histograms of the MODIS cloud-top height data, classified by TPW differences. Here, the frequencies on the vertical axis were normalized, and the analysis period is July and August 2018. In the region with the TPW difference $\Delta V \leq 2\ \mathrm{kg\,m^{-2}}$ (Fig. 15a), clouds with a cloud top of 1–2 km are the most frequent, while in the region with $2\ \mathrm{kg\,m^{-2}} < \Delta V < 4\ \mathrm{kg\,m^{-2}}$ (Fig. 15b), the percentage of lower clouds near the sea surface increases compared to Fig. 13a. Furthermore, in the region with the TPW difference $\Delta V \geq 4\ \mathrm{kg\,m^{-2}}$ (Fig. 15c), near-surface clouds or fog are most frequent, indicating that fog appears more frequently as the TPW differences increase.

Thus, we discussed the possible reason for the large TPW differences in the northwestern Pacific and northwestern Atlantic boreal summer. It was found that the TPW differences are large when the relative humidity in the lower atmosphere is close to 100% and the T_{1000} is higher than the SST. It was also found that a temperature inversion layer is likely to form in the lower atmosphere in a large TPW difference region. These meteorological conditions were observed most frequently in the boreal summer of the northwestern Pacific and northwestern Atlantic. These meteorological conditions are favorable for the development and maintenance of fog. The analyses and comparisons with MODIS data showed that the cloud or fog near the sea surface was more frequent in regions with larger TPW differences.

4.4 Influence of inversion layer and fog on the TPW algorithm

This section discusses the influence of inversion layers and sea fog on the JAXA and RSS TPW retrieval algorithm using a Radiative Transfer Model (RTM).

Correct information about the temperature profile is required to estimate TPW from the microwave brightness temperature observations precisely. However, temperature information cannot be obtained from AMSR2 observations. Thus, both TPW algorithms need to represent temperature profiles through LUTs or regression coefficients. As described in Section 2, the LUTs in the JAXA algorithm and the regression coefficients in the RSS algorithm are statistically determined using in-situ data, such as radiosonde observations, so they strongly reflect information from temperature profiles frequently observed by radiosonde. These temperature profiles are considered to have standard temperature lapse rates. That is, neither JAXA nor RSS algorithms can correctly represent a characteristic temperature lapse rate in an inversion layer.

As described in Section 2, the JAXA algorithm uses GANAL 850 hPa temperature data as auxiliary data, whereas the RSS algorithm does not use any auxiliary data and estimates SST simultaneously. For simplicity, we can approximate that the JAXA TPW algorithm assumes a temperature profile with a standard temperature lapse rate based on the GANAL 850 hPa air temperature and that the RSS TPW algorithm assumes a temperature profile with a standard temperature lapse rate based on surface air temperature consistent with the SST estimated simultaneously.

Based on the above approximation, sensitivity experiments were conducted with a simple atmospheric model including an inversion layer and fog. The green line in Fig. 16 represents the temperature profile with an inversion layer below 850 hPa (case I), similar to the temperature profiles of the reanalysis (Fig.12) and radiosonde (Fig.13). The temperature profile of case I has a standard temperature lapse rate of 6.5 K km^{-1} in the higher levels above 850 hPa. Here, we consider case I as the actual temperature profile with an inversion layer. In contrast to case I, the red line (case J) in Fig. 16 is a temperature profile with a lapse rate of 6.5 K km^{-1} and the same 850 hPa temperature values as case I. The blue line (case R) is a temperature profile with a lapse rate of 6.5 K km^{-1} and the same surface temperature values as case I. It can be considered that the temperature profile represented in the JAXA TPW algorithm is close to case J, and the temperature profile represented in the RSS TPW algorithm is close to case R. It should be noted that cases J and R were idealized to investigate the effect of the inversion layer, and we cannot know the actual temperature profiles assumed in the

JAXA and RSS algorithms. Figure 16 indicates that case J overestimates temperatures compared to case I in the lower atmosphere, while case R underestimates temperatures compared to case I for all altitudes. Figure 16 also shows profiles of water vapor and cloud water content. Water vapor has a simple profile that decreases exponentially in the upper layers, and the TPW value is 22.1 kg m^{-2}. In later sensitive experiments, the radiative transfer calculations were repeated, varying this water vapor profile by a constant factor. For cloud water, we assumed a uniform fog with a cloud particle size of 18 μm and a thickness of 1 km from the ground.

First, the brightness temperatures (TB) were calculated for the three temperature profiles (cases I, J, and R) by RTM. The TB differences from case I were examined for cases J and R, respectively. We used the Joint Simulator for Satellite Sensors (Hashino et al. 2013, 2016) as the RTM. The observation frequency and zenith angle of AMSR2 were assumed, and sea surface conditions such as SST and SSW are common. Here, we focused on the vertical polarization of TB at the three frequencies (18.7, 23.8, and 36.5 GHz) that were used mainly for the TPW retrieval algorithm (Kazumori et al. 2012). The TB for case I (TB_i) calculated from the case I air temperature, water vapor, and cloud water profiles shown in Fig. 16 can be considered as the TB observed by satellite under the actual atmospheric profile with an inversion layer. The TB for cases J (TB_j) and R (TB_r) were calculated from the temperature profiles of cases J and R, respectively. These first calculations used the same water vapor and cloud water profiles as in case I. The broken lines in Figs. 17a and b show the TB differences from TB_i for cases J (TB_j - TB_i) and R (TB_r - TB_i), respectively. Figure 17 shows that the

TB difference of 23.8 GHz is positively large in case J (Fig. 17a) and negatively large in case R (Fig. 17b). This can be interpreted that the overestimation of the lower-level temperature in case J leads to the overestimation of the radiative signal from the lower-level water vapor while the underestimation of the temperature in case R leads to the underestimation of the radiative signal from the water vapor.

In general, the TPW algorithm retrieves the TPW to be consistent with the observed TB (TBi in this case), so the TPW value when the TB errors from TBi is the smallest can be considered to be the optimal estimation of TPW under the assumption of temperature profiles for cases J and R, respectively. Therefore, the TB calculations for cases J (TB_j) and R (TB_r) were repeated, varying the water vapor profiles to minimize the TB errors from TBi. The errors were evaluated using the Root Mean Square of TB difference ($RMSTB = \sqrt{\frac{1}{3}\sum_{f=1}^{3}(TB_{j\ or\ r,f} - TB_{i,f})^2}$) from TBi at 18.7, 23.8, and 36.5 GHz. The water vapor profiles shown in Fig. 16 were increased or decreased by the same factor for all altitudes, and TPW was varied with an increment of 0.05 kg m^{-2}. Figures 17a and b show the TB differences ($TB_{j\ or\ r}$ - TB_i) at the minimum RMSTB for cases J and R, respectively. The RMSTB was minimized with a TPW of 21.9 kg m^{-2} for case J (solid red line) and 23.2 kg m^{-2} for case R (solid blue line). In the estimation of TPW (true value is 22.1 kg m^{-2}) from TB_i, the TPW is underestimated by the algorithm that assumes the case J temperature profile and is overestimated by the algorithm that assumes the case R temperature profile. Also, the absolute value of the TPW estimation error is larger in case R than in case J. This may be because case J overestimates the temperature only in the lower atmosphere, while case R underestimates the temperature over the entire altitude.

The above analysis was performed for idealized atmospheric profiles to investigate the effect of the inversion layer and sea fog. The TPW was underestimated in case J and was overestimated in case R. In addition, the TPW error estimation in case R was larger than that in case J. These results may explain why the JAXA products have a negative bias and the RSS products have a positive one from the radiosonde TPW (Fig. 6) and also why the absolute value of the bias for RSS was larger than that for the JAXA.

5. Summary

This study focused on comparisons and validations of the long-term AMSR2 total precipitable water (TPW) products estimated independently by the Japan Aerospace Exploration Agency (JAXA) and Remote Sensing Systems (RSS).

It was found that the TPW differences (RSS-JAXA) could be classified into two types: a small TPW difference independent of season and location, and a large TPW difference found in the boreal summer of the northwestern Pacific and northwestern Atlantic. We also compared JAXA and RSS TPW products with radiosonde water vapor observations for the global ocean and all seasons (case A) and the northwest Pacific and northwest Atlantic in boreal summer (case B). The JAXA and RSS TPW products had the opposite sign of biases for radiosonde observations. JAXA and RSS products have lower accuracy in case B than in case A. The differences in mean bias from radiosonde between

JAXA and RSS products were about 0.8 kg m^{-2} for case A and more than 2 kg m^{-2} for case B, consistent with the TPW difference in the time series analysis.

In addition to comparing the absolute values of the JAXA and RSS TPW products described above, we also compared the anomalies. The trend of TPW anomalies was calculated by subtracting the respective monthly mean values from both products. The results showed no significant differences in the global mean time series, water vapor trend values, or a regional dependence on water vapor trend.

The TPW differences in the northwest Pacific and northwest Atlantic for the boreal summer were more than 5 kg m^{-2} in some areas. This study investigated the meteorological conditions that caused these large TPW differences. The results were that the TPW differences were more likely to appear when the relative humidity in the lower atmosphere was close to 100%, the T_{1000} was higher than SST, and a surface inversion layer occurred in the lower atmosphere. It was found that such meteorological conditions occurred most frequently in the northwest Pacific and northwest Atlantic during the boreal summer. These conditions were also favorable to the development and maintenance of fog. Analysis of MODIS data showed that lower clouds or fog with the cloud tops near the sea surface were more frequent in regions with larger TPW differences.

Last, we discussed the influence of the inversion layer and sea fog on the JAXA and RSS TPW algorithms. Forward calculations of the RTM were performed with the simple atmospheric model including an inversion layer and fog while varying the TPW. This analysis suggested that the inversion layer was associated with the underestimation of TPW for the JAXA algorithm and the overestimation of TPW for the RSS algorithm. These results would explain the biases of opposite signs from radiosonde observations of the JAXA and RSS TPW products. Improving the JAXA TPW algorithm while considering the influence of an inversion layer is a subject for future study.

This study has focused only on AMSR2 data. AMSR2 has almost the same orbit and frequencies as AMSR-E, although the spatial resolution of AMSR2 is higher. AMSR-E observations are thus consistent with AMSR2 observations. However, the accurate evaluation of AMSR-E TPW still has issues related to the bias of brightness temperature (Geer et al. 2010), which will be addressed in the future. In addition, the GOSAT-GW satellite equipped with AMSR3 (the successor to AMSR2) (Kasahara et al. 2020) is currently scheduled for launch in FY2024. Consequently, the AMSR-E and the AMSR2 water vapor long-term dataset, combining AMSR3 observations, will become increasingly important. We will continue to validate the accuracy of AMSR-E and AMSR3 data to create a consistent long-term TPW dataset.

Data Availability Statement

JAXA AMSR2 Standard Product Level 2 ver. 2 and Level 3 ver. 2 data used in this study are available from the JAXA Satellite Data Distribution Site (G-Portal) (https://gportal.jaxa.jp/gpr/).

The RSS AMSR2 Daily products used in this study are available from their website (www.remss.com/missions/amsr.).

The radiosonde observations, objective analysis (GANAL), and MGDSST data used in this study are available from JMA. Restrictions apply to the availability of these data, which were used under an agreement between JAXA and JMA and are not publicly available. The data are available from the authors upon reasonable request, subject to permission from JMA.

The MODIS data used in this study are available from the Level-1 and Atmosphere Archive & Distribution System Distributed Active Archive Center (LAADS DAAC) (https://ladsweb.modaps.eosdis.nasa.gov/archive/allData/).

The Joint Simulator for Satellite Sensors is described at https://www.eorc.jaxa.jp/theme/Joint-Simulator/userform/js_userform.html.

Acknowledgments

The authors thank Dr. H. Murakami for helpful discussions and comments on the manuscript. JAXA AMSR2 Standard Product Level 2 ver. 2 and Level 3 ver. 2 data are available from the JAXA Satellite Data Distribution Site (G-Portal) (https://gportal.jaxa.jp/gpr/). RSS products are available from their website (Wentz, F.J., T. Meissner, C. Gentemann, K. A. Hilburn, J. Scott, 2014: Remote Sensing Systems GCOM-W1 AMSR2 Daily Environmental Suite on 0.25° grid, Version V. 8, Remote Sensing Systems, Santa Rosa, CA. Available online at www.remss.com/missions/amsr.). The Japan

Meteorological Agency provided the radiosonde observations, objective analysis (GANAL), and MGDSST data. MODIS data were obtained from the Level-1 and Atmosphere Archive & Distribution System Distributed Active Archive Center (LAADS DAAC) (https://ladsweb.modaps.eosdis.nasa.gov/archive/allData/). The Joint Simulator for Satellite Sensors is described at https://www.eorc.jaxa.jp/theme/Joint-Simulator/userform/js_userform.html.

References

Chen, B., and Z. Liu, 2016: Global water vapor variability and trend from the latest 36 year (1979 to 2014) data of ECMWF and NCEP reanalyses, radiosonde, GPS, and microwave satellite. *J. Geophys. Res.*, **121**, 11,442-11,462.

Dai, A., J. Wang, P. W. Thorne, D. E. Parker, L. Haimberger, and X. L. Wang, 2011: A New Approach to Homogenize Daily Radiosonde Humidity Data. *J. Clim.*, **24**, 965–991.

Geer, A. J., P. Bauer, and N. Bormann, 2010: Solar Biases in Microwave Imager Observations Assimilated at ECMWF. *IEEE Trans. Geosci. Remote Sens.*, **48**, 2660–2669.

Held, I. M., and B. J. Soden, 2000: Water vapor feedback and global warming. *Annu. Rev. Energy Environ.*, **25**, 441–475.

Hashino, T., M. Satoh, Y. Hagihara, T. Kubota, T. Matsui, T. Nasuno, and H. Okamoto, 2013: Evaluating cloud microphysics from NICAM against CloudSat and CALIPSO, J. Geophys. Res. Atmos., 118, 7273-7292, doi:10.1002/jgrd.50564.

Hashino, T., M. Satoh, Y. Hagihara, S. Kato, T. Kubota, T. Matsui, T. Nasuno, H. Okamoto, and M. Sekiguchi, 2016: Evaluating Cloud Radiative Effects in Arctic simulated by NICAM with A-train, J. Geophys. Res. Atmos., 121, 7041-7063, doi:10.1002/2016JD024775.

Imaoka, K., and Coauthors, 2010: Global Change Observation Mission (GCOM) for Monitoring Carbon, Water Cycles, and Climate Change. *Proc. IEEE*, **98**, 717–734.

IPCC, 2001: Climate Change 2001: The Scientific Basis. Contribution of Working Group I to the Third Assessment Report of the Intergovernmental Panel on Climate Change [Houghton, J.T., Y. Ding, D.J. Griggs, M. Noguer, P.J. van der Linden, X. Dai, K. Maskell, and C.A. Johnson (eds.)]. Cambridge University Press, Cambridge, United Kingdom, and New York, NY, USA, 881pp.

IPCC, 2007: Climate Change 2007: The Physical Science Basis. Contribution of Working Group I to the Fourth Assessment Report of the Intergovernmental Panel on Climate Change [Solomon, S., D. Qin, M. Manning, Z. Chen, M. Marquis, K. B. Averyt, M. Tignor and H.L. Miller (eds.)]. Cambridge University Press, Cambridge, United Kingdom, and New York, NY, USA, 996 pp.

IPCC, 2013: Climate Change 2013: The Physical Science Basis. Contribution of Working Group I to the Fifth Assessment Report of the Intergovernmental Panel on Climate Change [Stocker, T.F., D. Qin, G.-K. Plattner, M. Tignor, S.K. Allen, J. Boschung, A. Nauels, Y. Xia, V. Bex and P.M. Midgley (eds.)]. Cambridge University Press, Cambridge, United Kingdom, and New York, NY, USA, 1535 pp, doi:10.1017/CBO9781107415324.

IPCC, 2021: Climate Change 2021: The Physical Science Basis. Contribution of Working Group I to the Sixth Assessment Report of the Intergovernmental Panel on Climate Change [Masson-Delmotte, V., P. Zhai, A. Pirani, S.L. Connors, C. Péan, S. Berger, N. Caud, Y. Chen, L.

Goldfarb, M.I. Gomis, M. Huang, K. Leitzell, E. Lonnoy, J. B. R. Matthews, T.K. Maycock, T. Waterfield, O. Yelekçi, R. Yu, and B. Zhou (eds.)]. Cambridge University Press, Cambridge, United Kingdom, and New York, NY, USA, In press, doi:10.1017/9781009157896.

Kasahara, M., M. Kachi, K. Inaoka, H. Fujii, T. Kubota, R. Shimada, and Y. Kojima, 2020: Overview and current status of GOSAT-GW mission and AMSR3 instrument. *Sensors, Systems, and Next-Generation Satellites XXIV*, Vol. 11530 of, Sensors, Systems, and Next-Generation Satellites XXIV, SPIE, 1153007 (Accessed July 8, 2022).

Kawanishi, T., and Coauthors, 2003: The Advanced Microwave Scanning Radiometer for the Earth Observing System (AMSR-E), NASDA's contribution to the EOS for global energy and water cycle studies. *IEEE Trans. Geosci. Remote Sens.*, **41**, 184–194.

Kazumori, M., T. Egawa, and K. Yoshimoto, 2012: A retrieval algorithm of atmospheric water vapor and cloud liquid water for AMSR-E. *European Journal of Remote Sensing*, **45**, 63–74.

Kidd, C., G. Huffman, V. Maggioni, P. Chambon, and R. Oki, 2021: The Global Satellite Precipitation Constellation: Current Status and Future Requirements. *Bull. Am. Meteorol. Soc.*, **102**, E1844–E1861.

Klein, S. A., and D. L. Hartmann, 1993: The Seasonal Cycle of Low Stratiform Clouds. *J. Clim.*, **6**, 1587–1606.

Kubar, T. L., D. E. Waliser, J.-L. Li, and X. Jiang, 2012: On the Annual Cycle, Variability, and Correlations of Oceanic Low-Topped Clouds with Large-Scale Circulation Using Aqua MODIS and ERA-Interim. *J. Clim.*, **25**, 6152–6174.

Mears, C. A., D. K. Smith, L. Ricciardulli, J. Wang, H. Huelsing, and F. J. Wentz, 2018: Construction and uncertainty estimation of a satellite-derived total precipitable water data record over the world's oceans. *Earth Space Sci.*, **5**, 197–210.

Mieruch, S., S. Noël, and H. Bovensmann, 2008: Analysis of global water vapour trends from satellite measurements in the visible spectral range. *Chem. Phys. Lipids*., **8**, 491–504, https://doi.org/10.5194/acp-8-491-2008

Mieruch, S., M. Schröder, S. Noël, and J. Schulz, 2014: Comparison of decadal global water vapor changes derived from independent satellite time series. *J. Geophys. Res.*, **119**, https://doi.org/10.1002/2014jd021588.

Miller, M. A., and S. E. Yuter, 2013: Detection and characterization of heavy drizzle cells within subtropical marine stratocumulus using AMSR-E 89-GHz passive microwave measurements. *Atmos. Meas. Tech*., **6**, 1-13, https://doi.org/10.5194/amt-6-1-2013, 2013.

Nilsson, T., and G. Elgered, 2008: Long-term trends in the atmospheric water vapor content estimated from ground-based GPS data. *J. Geophys. Res.*, **113**, https://doi.org/10.1029/2008jd010110.

Norris, J. R., and C. B. Leovy, 1994: interannual Variability in Stratiform Cloudiness and Sea Surface Temperature. *J. Clim.*, **7**, 1915–1925.

—, and S. F. Iacobellis, 2005: North Pacific Cloud Feedbacks Inferred from Synoptic-Scale Dynamic and Thermodynamic Relationships. *J. Clim.*, **18**, 4862–4878.

Ross, R. J., and W. P. Elliott, 2001: Radiosonde-Based Northern Hemisphere Tropospheric Water Vapor Trends. *J. Clim.*, **14**, 1602–1612.

Sakurai, T., K. Yukio, and T. Kuragano, 2005: Merged satellite and in-situ data global daily SST. *Proceedings. 2005 IEEE International Geoscience and Remote Sensing Symposium, 2005. IGARSS '05.*, Vol. 4 of, ieeexplore.ieee.org, 2606–2608.

Schröder, M., M. Lockhoff, J. M. Forsythe, H. Q. Cronk, T. H. Vonder Haar, and R. Bennartz, 2016: The GEWEX Water Vapor Assessment: Results from Intercomparison, Trend, and Homogeneity Analysis of Total Column Water Vapor. *J. Appl. Meteorol. Climatol.*, **55**, 1633–1649.

—, and Coauthors, 2018: The GEWEX Water Vapor Assessment archive of water vapour products from satellite observations and reanalyses. *Earth Syst Sci Data*, **10**, 1093–1117.

—, and Coauthors, 2019: The GEWEX Water Vapor Assessment: Overview and Introduction to Results and Recommendations. *Remote Sensing*, **11**, 251.

Trenberth, K. E., A. Dai, R. M. Rasmussen, and D. B. Parsons, 2003: The Changing Character of Precipitation. *Bull. Am. Meteorol. Soc.*, **84**, 1205–1218.

—, J. T. Fasullo, and J. Kiehl, 2009: Earth's Global Energy Budget. *Bull. Am. Meteorol. Soc.*, **90**, 311–324.

Wagner, T., S. Beirle, M. Grzegorski, and U. Platt, 2006: Global trends (1996–2003) of total column precipitable water observed by Global Ozone Monitoring Experiment (GOME) on ERS-2 and their relation to near-surface temperature. *J. Geophys. Res.*, **111**, https://doi.org/10.1029/2005jd006523.

Wang, J., L. Zhang, A. Dai, and T. Van Hove, 2007: A near‐global, 2‐hourly data set of atmospheric precipitable water from ground‐based GPS measurements. *Journal of*, https://doi.org/10.1029/2006JD007529.

Wang, J., A. Dai, and C. Mears, 2016: Global Water Vapor Trend from 1988 to 2011 and Its Diurnal Asymmetry Based on GPS, Radiosonde, and Microwave Satellite Measurements. *J. Clim.*, **29**, 5205–5222.

Wentz, F. J., 2000: Algorithm Theoretical Basis Document (ATBD) AMSR Ocean Algorithm (Version 2). RSS Tech. Proposal 121599A-1, Remote Sensing Systems, Santa Rosa, CA. *http://www.ssmi.com/tmiInfo.html.*,.

—, and M. Schabel, 2000: Precise climate monitoring using complementary satellite data sets. *Nature*, **403**, 414–416.

Wentz, F. J. and T. Meissner, 2007: AMSR-E Ocean Algorithms; Supplement 1, report number 051707, 6 pp., Remote Sensing Systems, Santa Rosa, CA.

Wentz, F. J., L. Ricciardulli, K. Hilburn, and C. Mears, 2007: How much more rain will global warming bring? *Science*, **317**, 233–235.

Zhai, P., and R. E. Eskridge, 1997: Atmospheric Water Vapor over China. *J. Clim.*, **10**, 2643–2652.

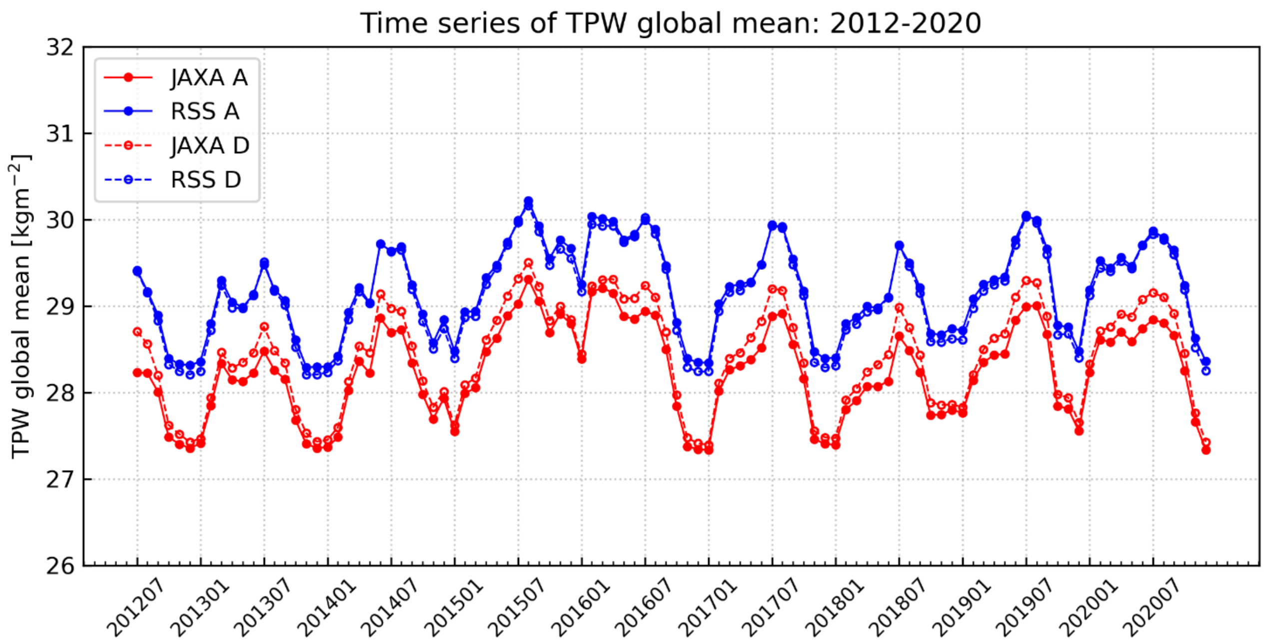

Fig. 1 Time series of the global monthly mean of AMSR2 TPW for JAXA and RSS over the ocean from July 2012 to December 2020. The solid lines represent the ascending orbit data (13:30 local time), and the broken lines represent the descending orbit data (01:30 local time).

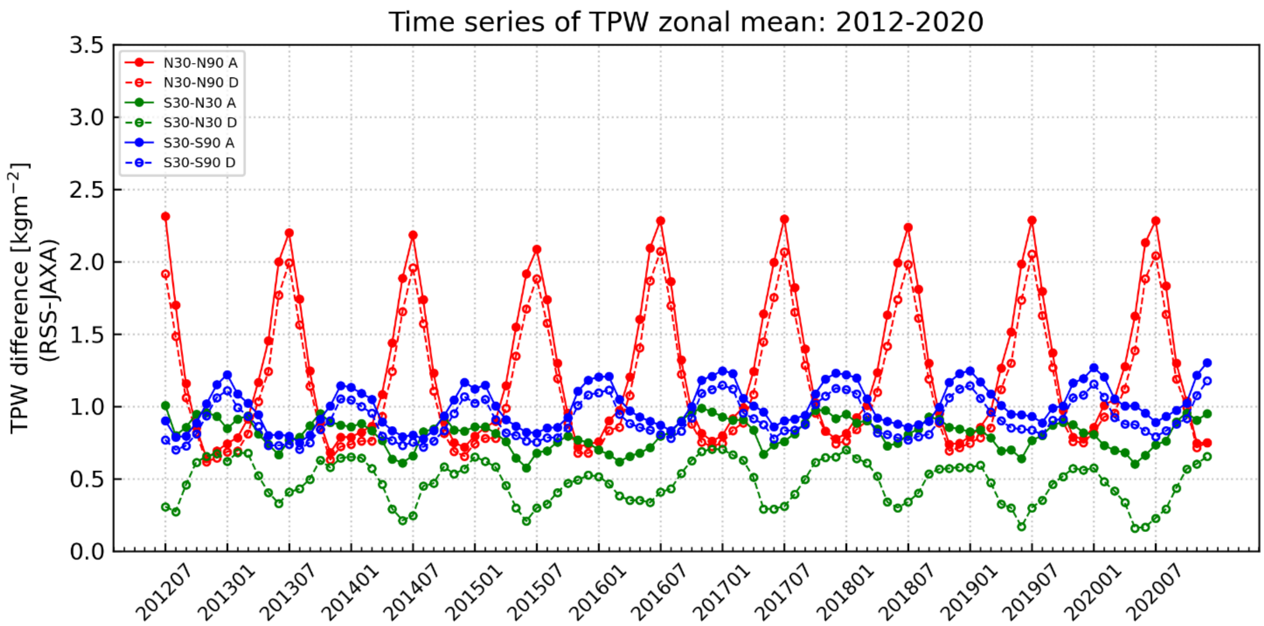

Fig. 2 Time series of the difference of the latitudinal zonal mean of TPW between RSS and JAXA.

The latitudinal zonal means are classified by the northern hemisphere's mid-high latitudes (30º–60° N), the tropics (30° S–30° N), and the southern hemisphere's mid-high latitudes (30-60°S).

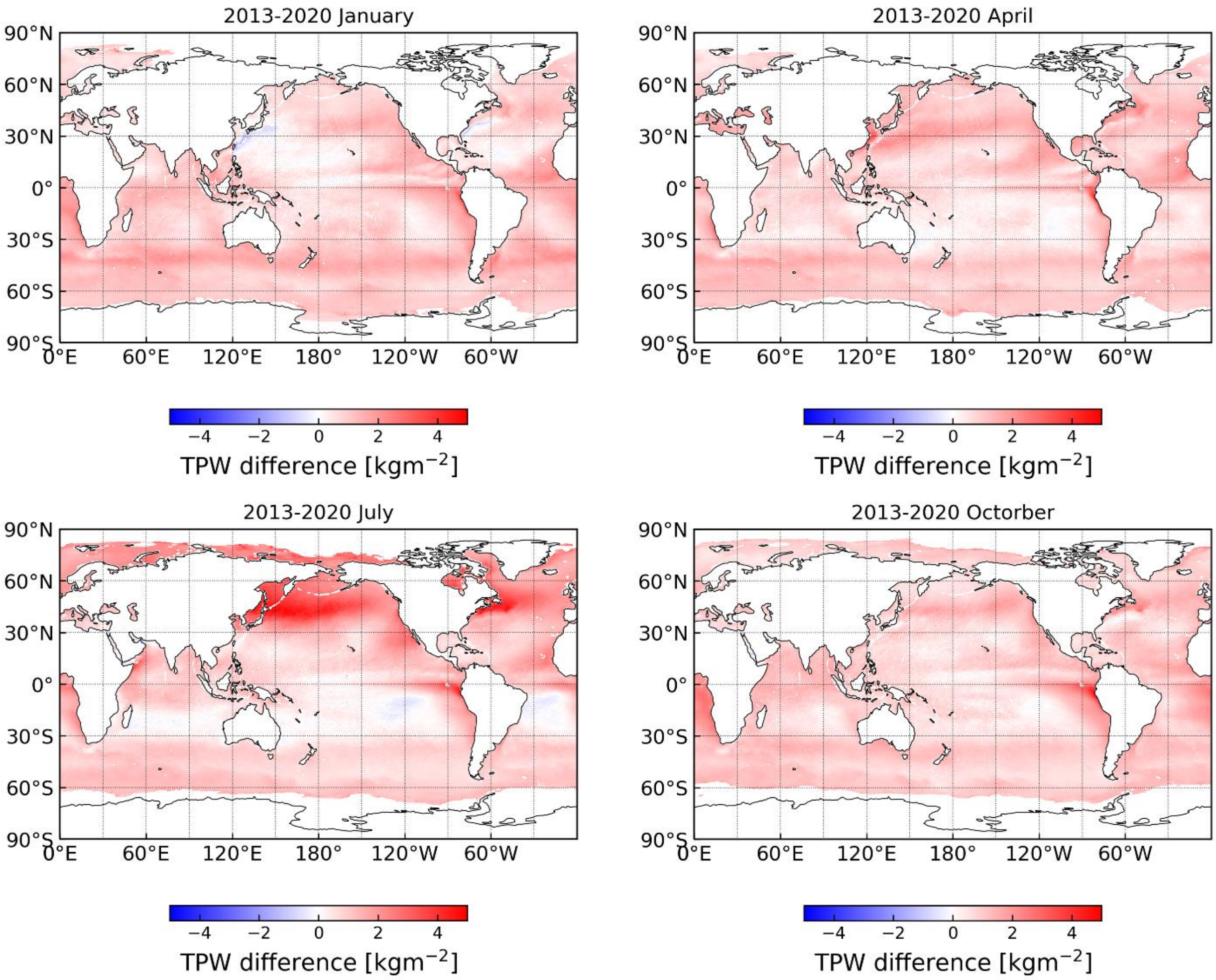

Fig. 3 Horizontal distribution of TPW differences averaged over January, April, July, and October for 2013–2020.

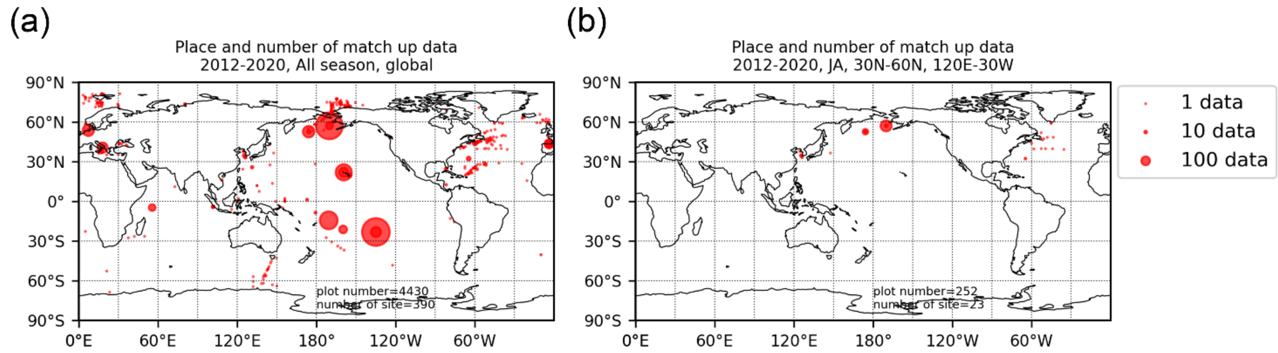

Fig. 4 Distribution of the matched data between AMSR2 TPW (JAXA and RSS) and radiosonde observation for (a) global comparison during all seasons of 2012–2020 and (b) the northwest Pacific and northwest Atlantic (30º-60º N, 120º E-30º W) Oceans during the summer (July and August) of 2012–2020.

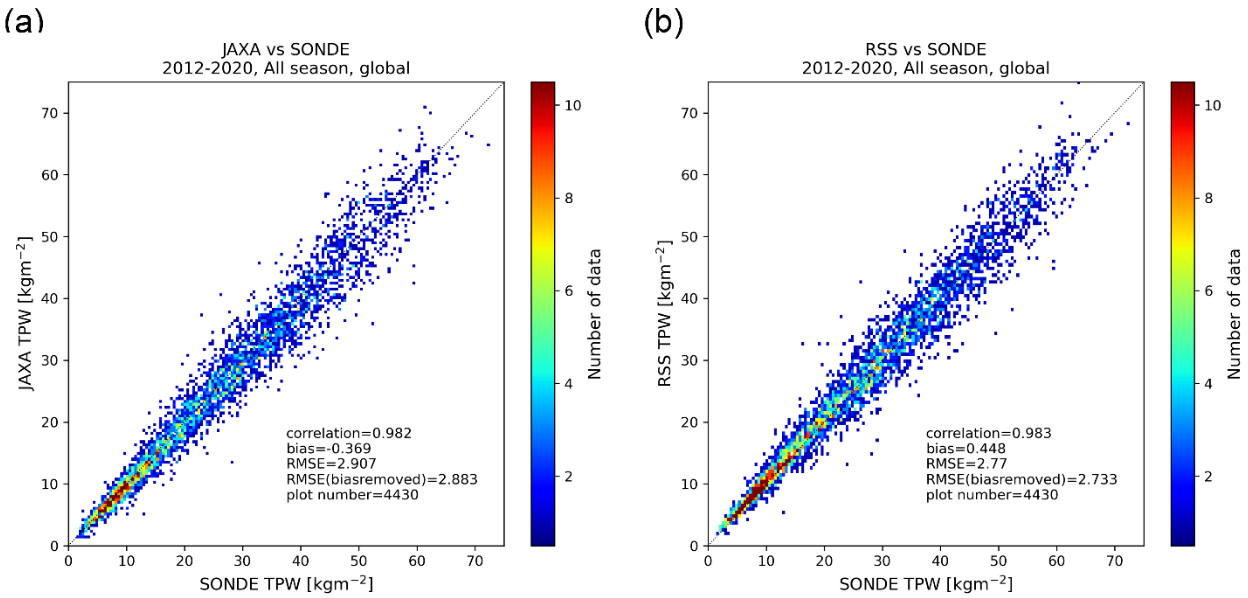

Fig. 5 Global comparison of radiosonde and AMSR2 L3 TPW products of (a) JAXA and (b) RSS for all seasons of 2012–2020. The value of the color bar indicates the number of matchup data that fall into the same bin.

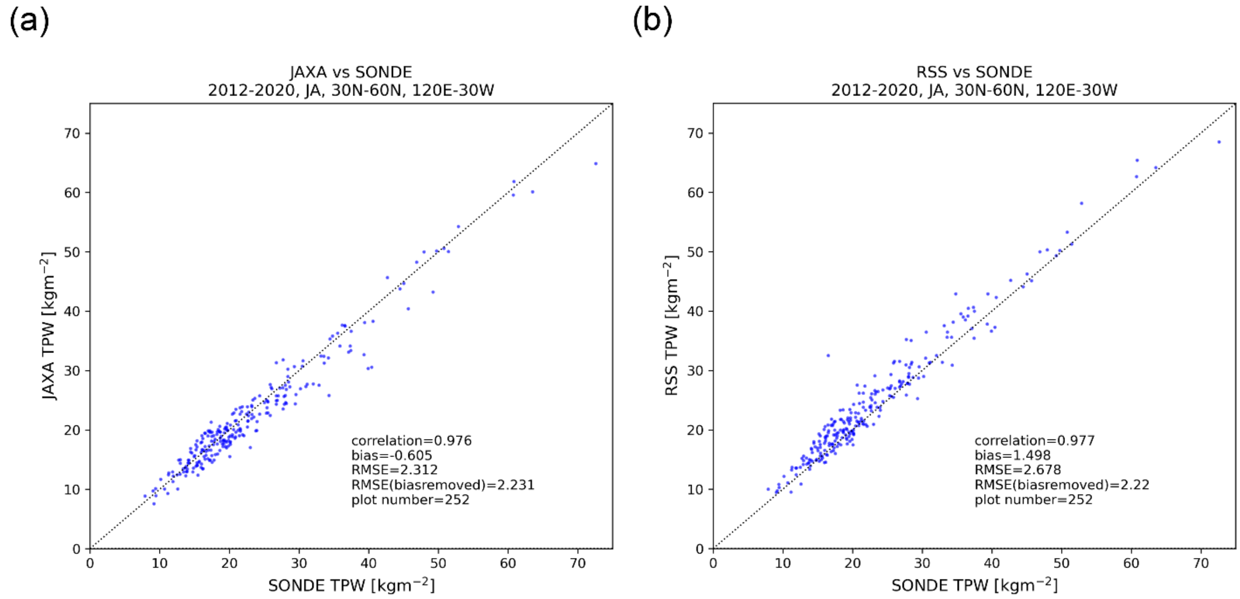

Fig. 6 Comparison of radiosonde and AMSR2 L3 TPW products of (a) JAXA and (b) RSS in the northwest Pacific and northwest Atlantic Oceans (30º–60º N, 120º E–30º W) during the summer (July and August) of 2012–2020.

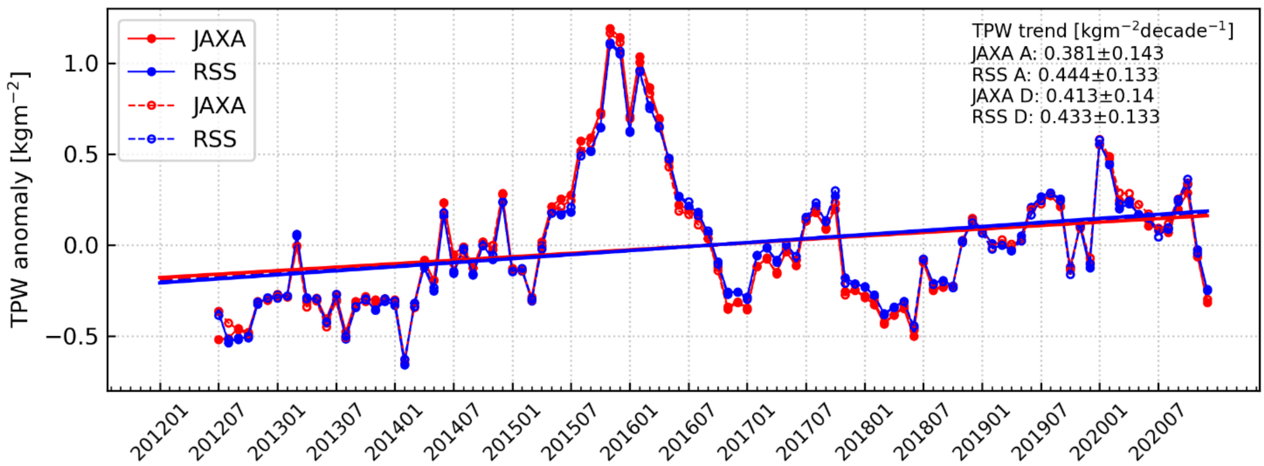

Fig. 7 Time series of the anomalies of the TPW global mean for JAXA and RSS products. The linear regression lines and their slopes [kg m^{-2} decade^{-1}] are also shown.

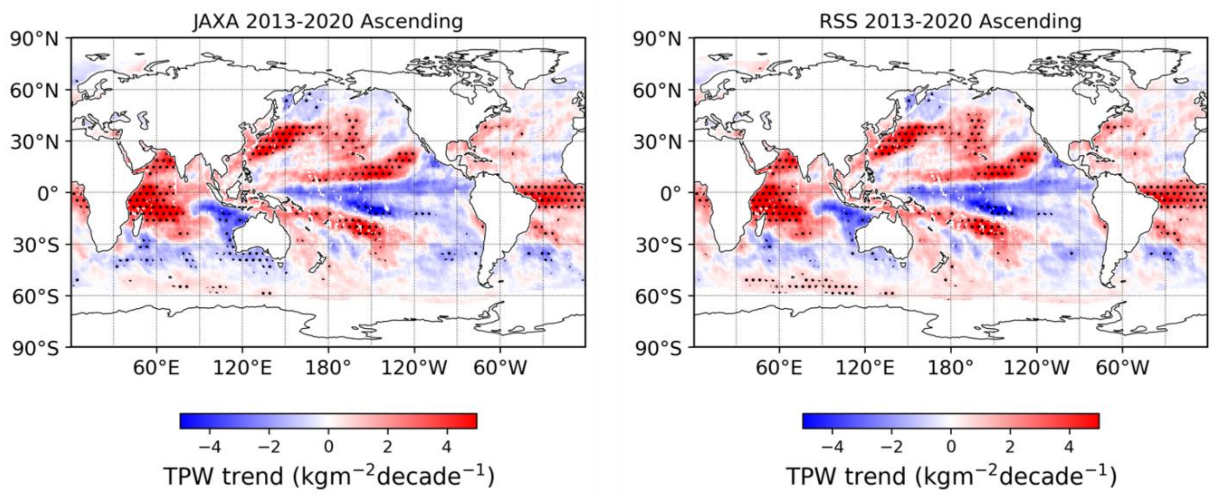

Fig. 8 Horizontal distribution of water vapor trends of JAXA and RSS TPW products. The dotted regions indicate significant trends at the 95% confidence level calculated by the t-test.

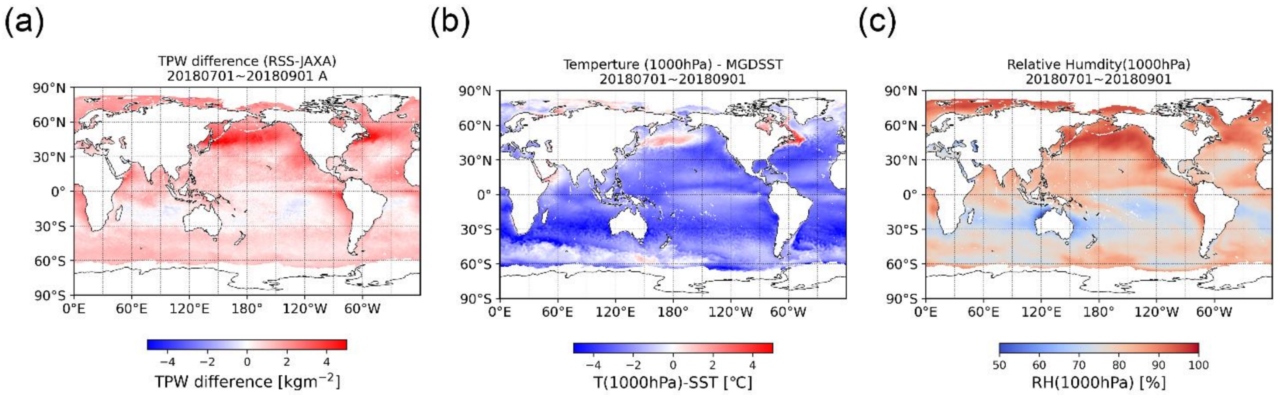

Fig. 9 Horizontal distributions of (a) TPW difference, (b) T_{1000}-SST, and (c) RH_{1000} for July and August 2018.

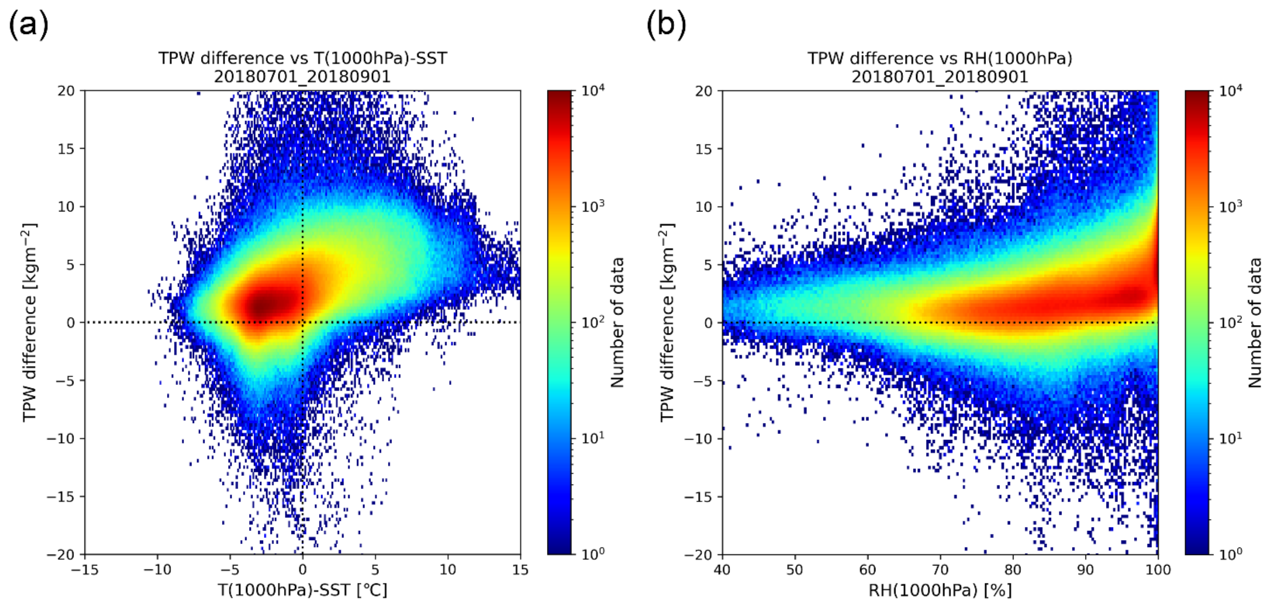

Fig. 10 Scatter plots of the relationship (a) between TPW difference and T_{1000}-SST and (b) between TPW difference and RH_{1000}, using the 30º–60° N region data for July and August 2018. The value of the color bar indicates the number of data that fall into the same bin.

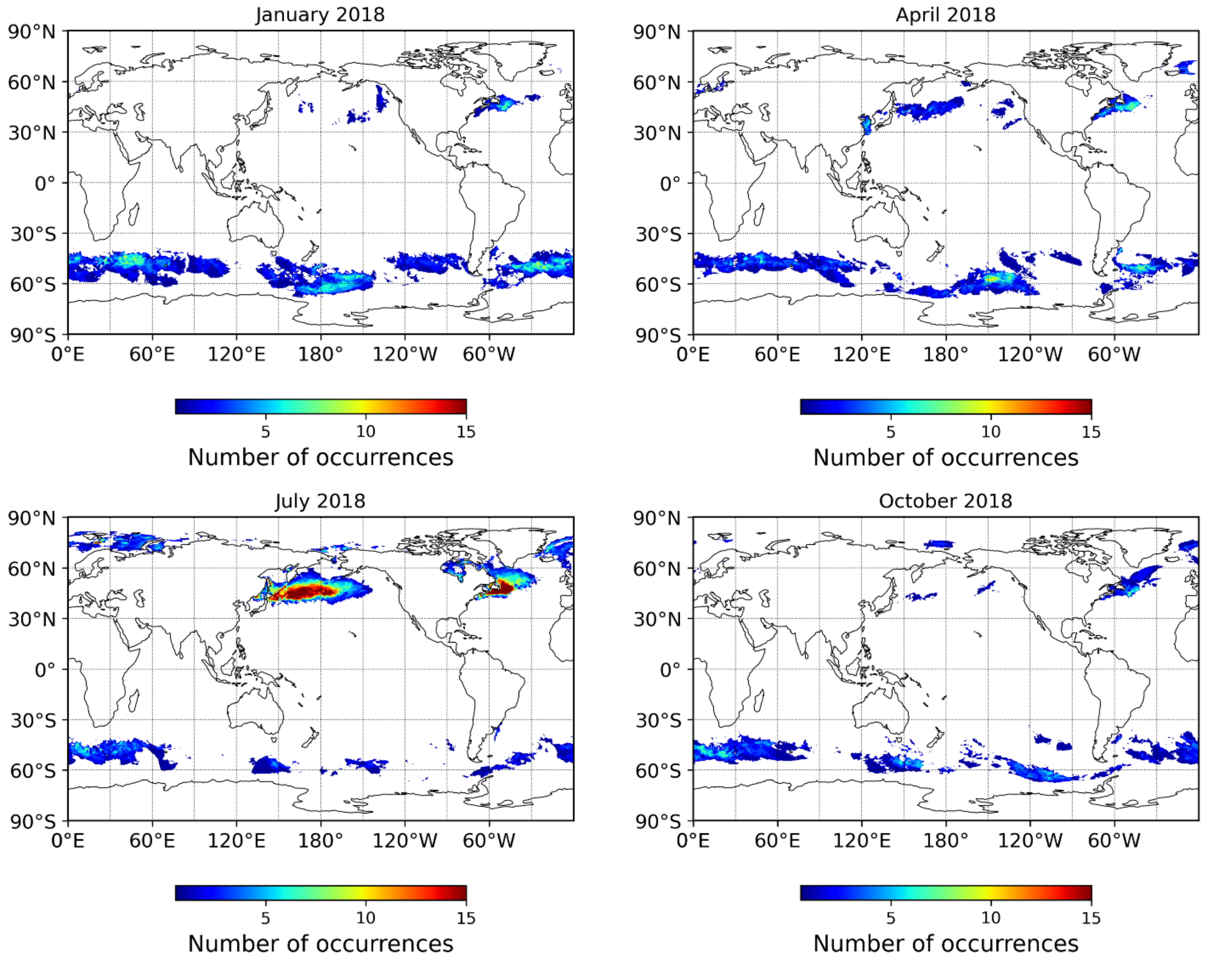

Fig. 11 The seasonal and regional dependences of the frequency of the cases which satisfy T_{1000}-SST > 2°C and RH_{1000}>95% in January, April, July, and October 2018. The value of the color bar indicates the number of occurrences for each grid.

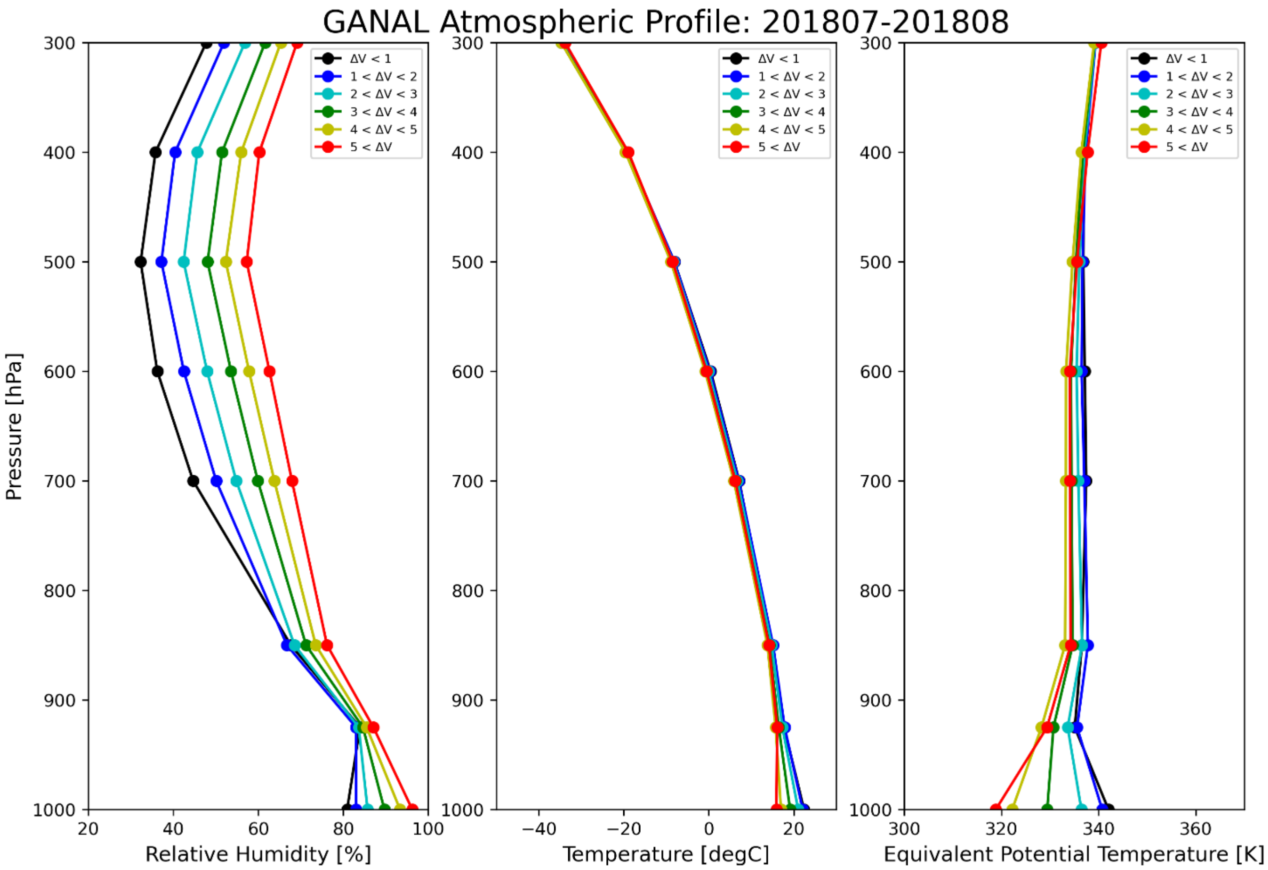

Fig. 12 Averaged atmospheric vertical profiles in the 30º–60° N region for July and August 2018. The atmospheric vertical profiles are classified by TPW difference values: ΔV>5 (red), 4<ΔV<5 (yellow), 3<ΔV<4 (green), 2<ΔV<3 (light blue), 1<ΔV<2 (blue) and ΔV<1 (black).

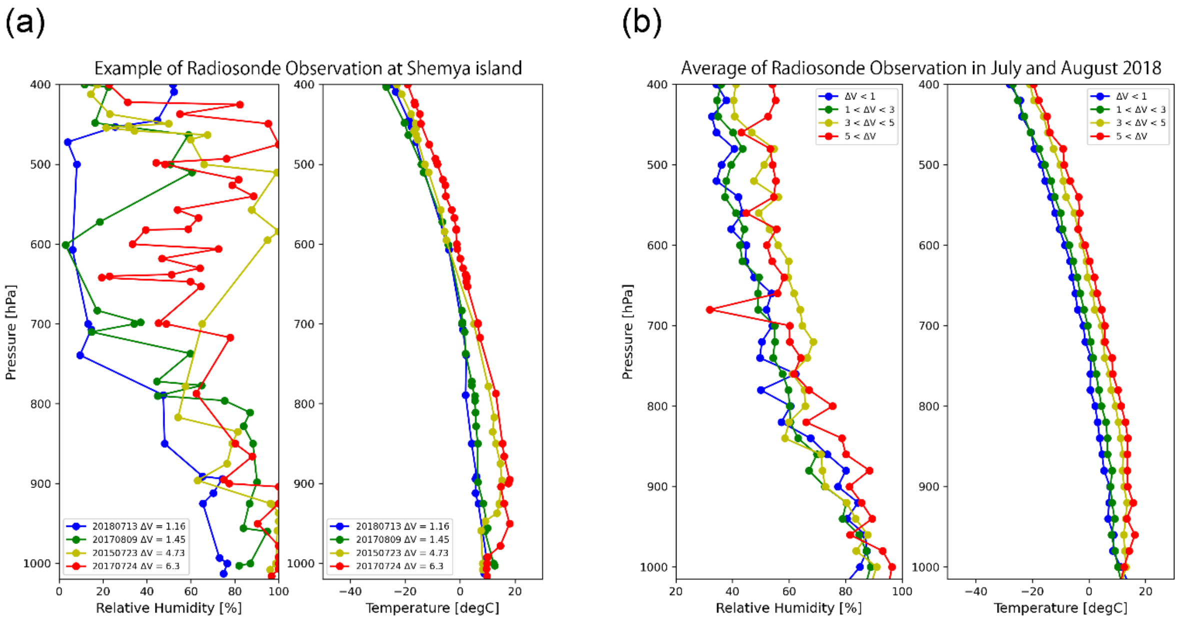

Fig. 13 (a) Example of the radiosonde atmospheric profiles. The observation date and TPW difference ΔV are shown in the legend. (b) Average of the radiosonde atmospheric profiles in the summer (July and August) of 2012–2020 for the Northwest Pacific and Northwest Atlantic (30º–60 N, 120º E–30º W). The atmospheric vertical profiles are classified by the TPW difference: ΔV>5 (red), 3<ΔV<5 (yellow), 1<ΔV<3 (green), and ΔV<1 (blue).

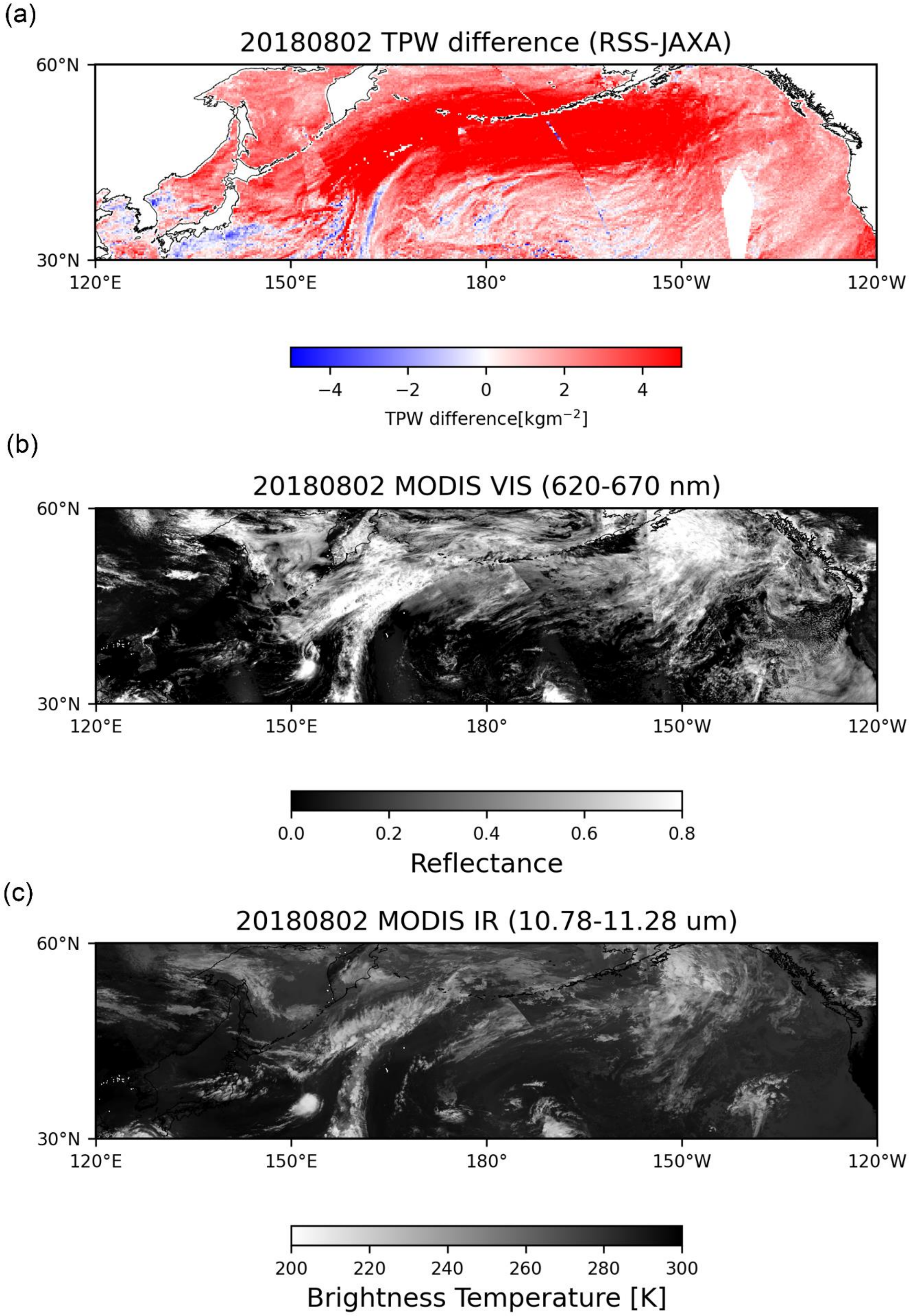

Fig. 14 Daily merged images of (a) AMSR2 TPW difference (RSS-JAXA) and (b) MODIS visible (0.62−0.67 μm) and (c) infrared (10.78−11.28 μm) on August 2, 2018.

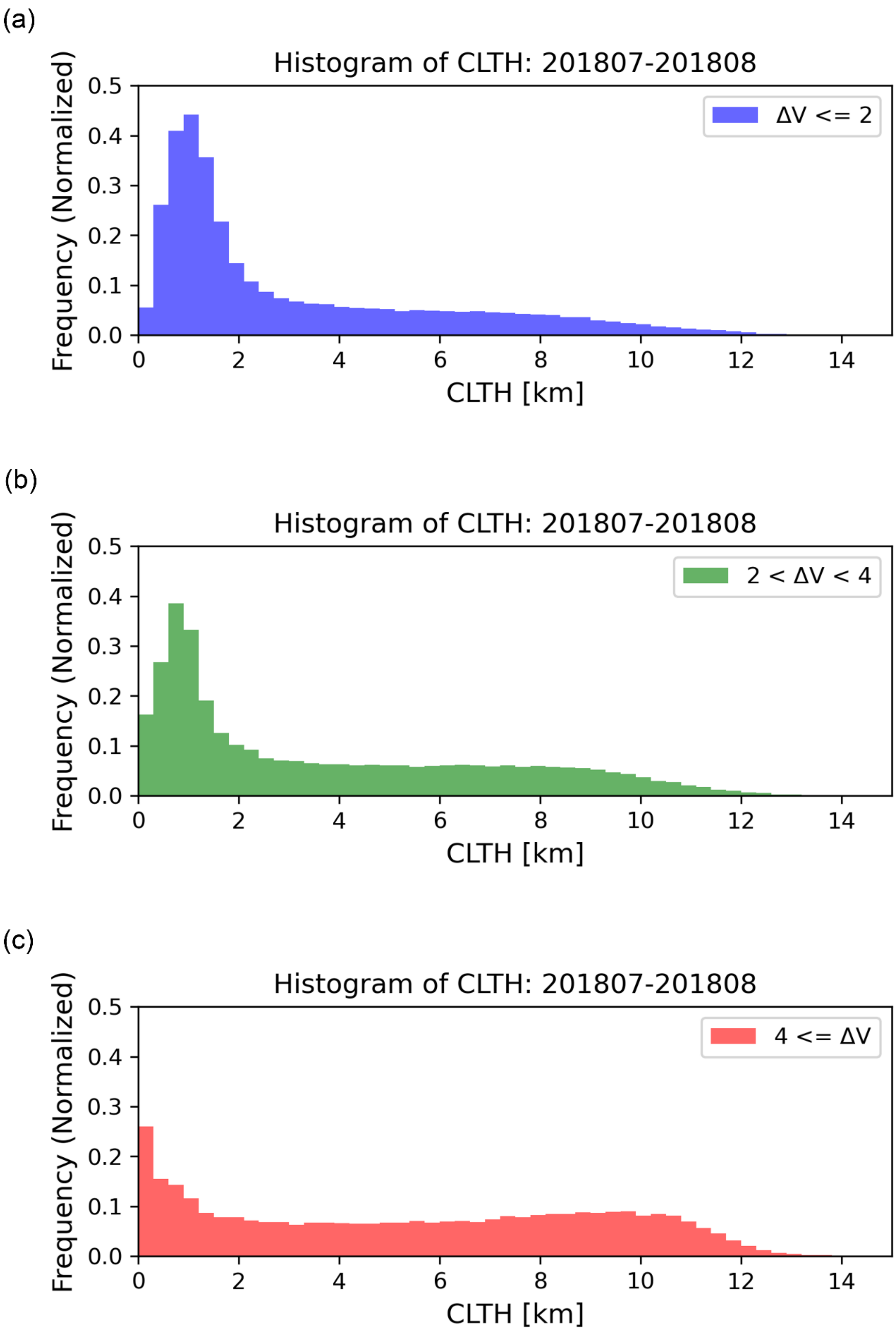

Fig. 15 Histograms of the cloud top height (CLTH) obtained by MODIS products in July and August

2018, classified by TPW differences (RSS-JAXA) ΔV [kg m^{-2}]: (a) ΔV<2, (b) 2<ΔV<4, (c) ΔV>4.

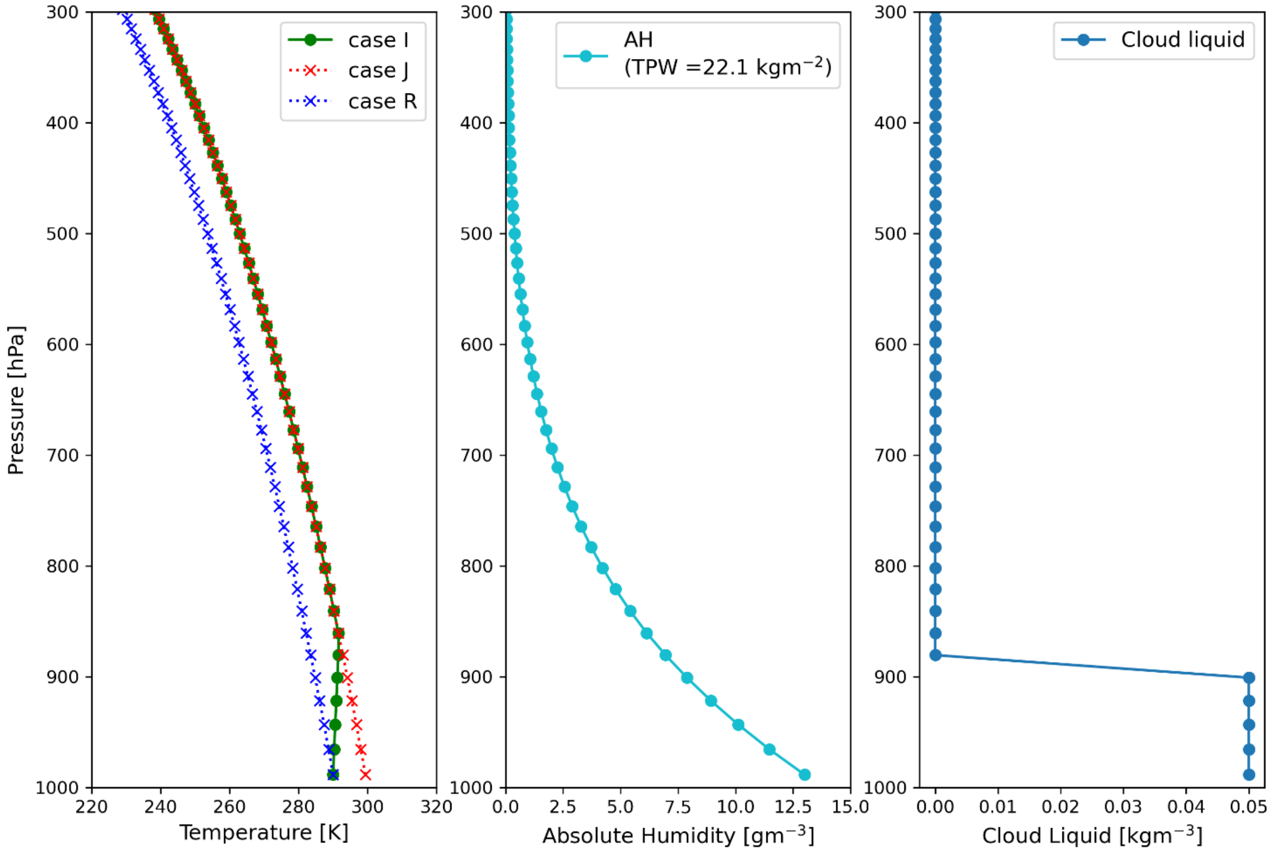

Fig. 16 Atmospheric vertical profiles for the radiative transfer calculations by the Joint Simulator for Satellite Sensors.

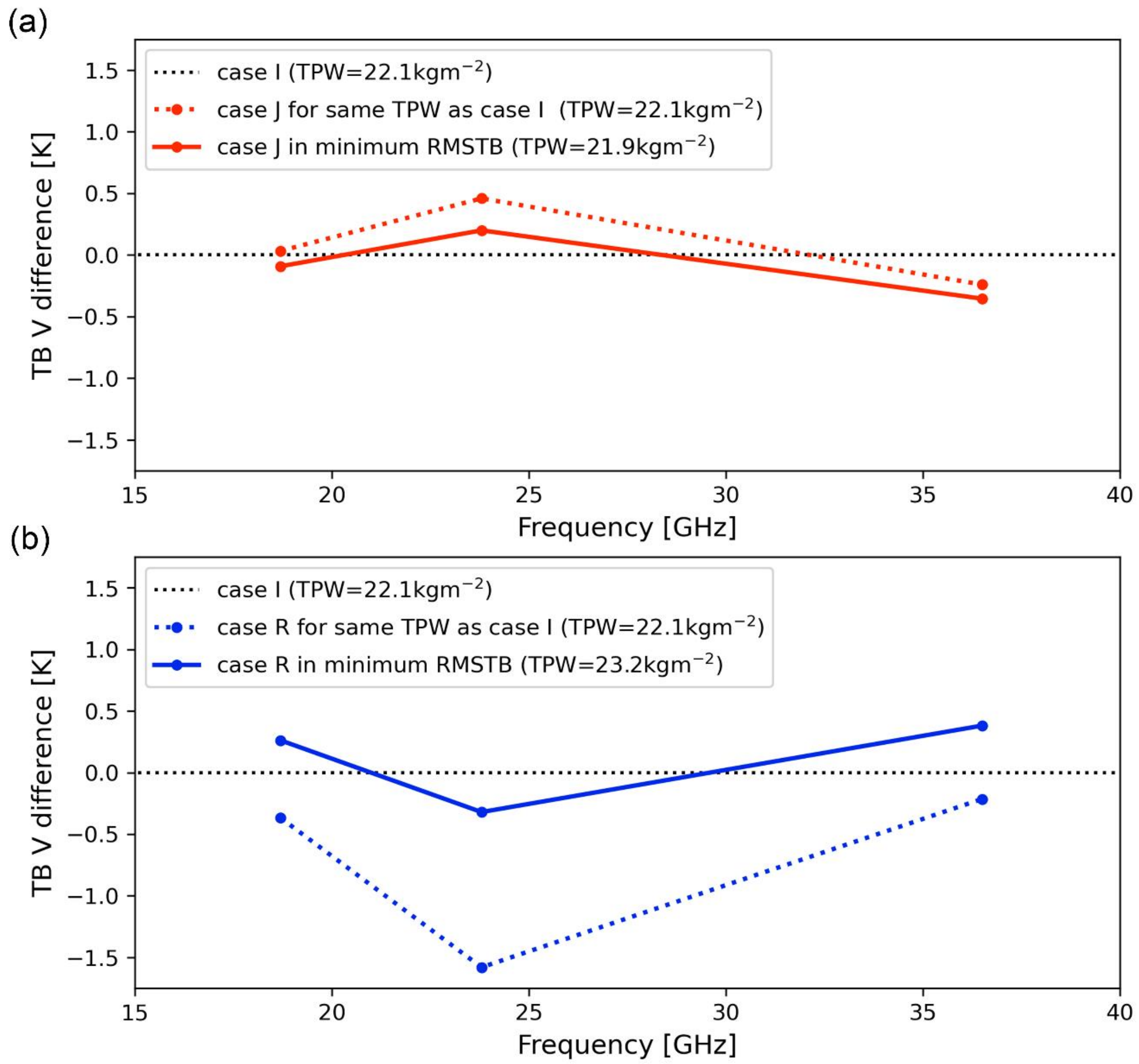

Fig. 17 Results of sensitivity analysis. TPW dependences of the TB difference for (a) TB in case J – TB in case I and (b) TB in case R- TB in case I at three frequencies (18.7, 23.8, and 36.5 GHz).

Table 1. Comparison of radiosonde observations with AMSR2 TPW (JAXA and RSS)

	Bias [kg/m^2]	RMSE [kg/m^2]	RMSE (bias removed) [kg/m^2]	No. of data
JAXA (Global, All period)	-0. 369	2.907	2.883	4430
RSS (Global, All period)	0. 448	2.770	2.733	4430
JAXA (30º–60ºN JA)	-0.605	2.312	2.231	252
RSS (30º–60ºN JA)	1.498	2.678	2.220	252

Table 2. Pattern correlation coefficient with TPW difference (RSS-JAXA) and other geophysical parameters

Data	CLW (JAXA)	CLW difference (RSS-JAXA)	MGD SST	SST difference (MGDSST-RSS SST)	GANAL SSW	SSW difference (GANAL - RSS SSW)	GANAL T_{1000}-MGDSST	GANAL RH_{1000}
Pattern Correlation Coefficient (Global)	0.15	0.04	-0.25	0.18	-0.13	-0.43	0.53	0.74
Pattern Correlation Coefficient (30–60º N)	0.55	0.26	-0.61	-0.27	0.41	-0.61	0.71	0.69